DOI 10.1007/s11141-015-9588-z
*Radiophysics and Quantum Electronics, Vol. 58, No. 2, July, 2015*
*(Russian Original Vol. 58, No. 2, February, 2014)*

# NEAR-FIELD TOMOGRAPHY AND HOLOGRAPHY OF LOW-CONTRAST SUBSURFACE OBJECTS

**K. P. Gaikovich**[1,2] * **and E. S. Maksimovich**[2]

UDC 621.396.967

*We develop a new method for electromagnetic computer tomography of distributed subsurface inhomogeneities and holography (i.e., retrieval of the form) of internally homogeneous subsurface objects. The method is based on solving the inverse problem of near-field scattering with allowance for the data of multifrequency measurements of the two-dimensional distribution of the scattered-field complex amplitudes along the medium surface over the region of inhomogeneities.*

## 1. INTRODUCTION

The purpose of tomography, i.e., in this case, obtaining the three-dimensional distribution of the dielectric permittivity in a medium with a surface inhomogeneity, consists in solving the inverse scattering problem based on the data of multifrequency measurements of the microwave field scattered by dielectric objects at a depth comparable with the penetration depth of the near field for the longest wavelength in the frequency band of the probing signal. Near-field measurements are attractive due to the possibility of going beyond the Rayleigh resolution limit, which is the only way in the case where the transition to a shorter-wavelength band is impossible due to an increase in the wave attenuation in a medium.

Solution of such three-dimensional problems on the basis of the Maxwell equations is related to severe restrictions imposed on the dimension of the analysis grid and, consequently, the rigid constraint on the achievable resolution. Therefore, in some works, approaches have been proposed according to which the nonlinear integral equation, which is equivalent to the Maxwell equations with boundary conditions, is reduced to the one-dimensional integral equation for the transverse (to the line of sight) spatial-inhomogeneity spectrum and then solved repeatedly for each pair of spectral components. This reduction, which is based on the two-dimensional Fourier transform with respect to the coordinates transverse to the line of sight, is not always possible since in the general case, the initial equation is not a convolution equation and admits such a representation in some cases only. In this respect, we can mention the methods developed for microwave radiometry and impedance diagnostics, for low-frequency sounding of the Earth's crust, and the method based on measuring the scattering of the wave field, which penetrates into a medium in the case of total internal reflection, from a subsurface inhomogeneity [1, 2].

Herein, we develop an approach based on the scheme of measurements [3] which are performed in the two-dimensional region over the inhomogeneity by a rigidly bound source–receiver system. Depth sensitivity is ensured by measurements depending on the third parameter, such as signal frequency, or diameter of the receiving-antenna aperture, or height of the scanning level. This scheme transforms the three-dimensional equation in the Born approximation to a convolution equation reduced to a one-dimensional

* gai@ipm.sci-nnov.ru

[1] Institute for Physics of Microstructures of the Russian Academy of Sciences; [2] N. I. Lobachevsky State University of Nizhny Novgorod, Nizhny Novgorod, Russia; [3] Institute of Applied Physics of the National Academy of Sciences, Minsk, Belarus. Translated from Izvestiya Vysshikh Uchebnykh Zavedenii, Radiofizika, Vol. 58, No. 2, pp. 142–156, February 2014. Original article submitted April 3, 2014; accepted June 30, 2014.

 

integral equation, which should be solved for each pair of wave numbers in the two-dimensional spectrum transverse to the line of sight. Moreover, this approach allows one to obtain a certain correction to the solution in the Born approximation. The transverse spatial spectra of the Green's functions, which form the kernel of the solved equation, were obtained in explicit form in [3]. In that work, the method for solving such Fredholm equations of the first kind for complex-valued functions in the Sobolev space $W_2^1$ on the basis of the generalized-residual principle was also tested.

This approach was experimentally realized as a method of subsurface microwave tomography of inhomogeneities in soil [4]. Analyzing the results of the experiment, we faced difficulties in discerning the subsurface scattering signal against the background of strong contribution made by the scattering from the surface. We managed to overcome these difficulties by transforming multifrequency data to a synthesized complex pseudo-pulse, in which these contributions were separated effectively. The equation to be solved was transformed to this new formulation of the problem, and good results of the tomography of distributed and spatially limited test inhomogeneities were obtained.

It should be noted that the shape of the surface is a determining characteristic for internally homogeneous and spatially limited objects, which occur in practice much more frequently than inhomogeneous objects. However, the determination of the shape (the task of computer holography), based on the results of solving a more general tomography problem, is not a trivial problem, as will be shown in what follows. The approach to solving the problem of holography of such object and the first results are also described in [4]. To a certain extent, similar approaches are currently developed with the purpose of obtaining radio holography images of surfaces of metal inhomogeneities [5].

In this work, the above-described method of tomography and holography is studied on the basis of both numerical and full-scale experiments.

## 2. INVERSE PROBLEM OF SCATTERING IN A MULTILAYER MEDIUM

Although in this work we consider the problem for the case of probing inhomogeneities in a homogeneous half-space, the proposed method is valid for a significantly more general case of a multilayer medium if the measuring system and the probed inhomogeneity are located in different layers. For example, let the probing system be located in the $k$th layer (the layers are numbered in the $z$ direction) with the complex dielectric permittivity $\varepsilon = \varepsilon_{0k}$ and magnetic permeability $\mu = \mu_{0k}$ and the probed inhomogeneity, in the $l$th layer with $\varepsilon = \varepsilon_{0l}$ and $\mu = \mu_{0l}$. Then, the distribution of the complex dielectric permittivity in the $l$th layer is represented as a sum of the constant component of the dielectric permittivity of the medium in this layer and the three-dimensional inhomogeneity of the medium, whose distribution should be retrieved from the measurements of $\varepsilon(\mathbf{r}) = \varepsilon_{0l} + \varepsilon_1(\mathbf{r})$. The complex amplitudes of the total field measured in the $k$th layer in the two-dimensional region $(x, y)$ at the frequency $\omega$ are determined by the sum of the components of the probing and scattered fields: $\mathbf{E}(x, y, z, \omega) = \mathbf{E}_0(x, y, z, \omega) + \mathbf{E}_1(x, y, z, \omega)$. The scattered field $\mathbf{E}_1$ is determined by the distribution $\varepsilon_1(\mathbf{r})$ of the inhomogeneity by means of the three-dimensional integral Fredholm equation of the second kind. It was shown in [3] that for the measurement scheme with a rigidly bound system of a source and a receiver the distance between which is specified by the vector $\delta\mathbf{r}$, this integral equation in the Born approximation has the form of a convolution with respect to the transverse coordinates $x$ and $y$. The form of this equation allows one to use the two-dimensional Fourier transform to obtain a one-dimensional integral equation for each pair of the components $k_x$ and $k_y$ of the scattered-field spectrum transverse to the line of sight:

$$E_{1i}(k_x, k_y, \omega, z, \delta\mathbf{r}) = -4\pi^3 i\omega \int\limits_{-\infty}^{0} \varepsilon_1(k_x, k_y, z') \left\{ \iint\limits_{-\infty}^{+\infty} \exp(-i\kappa_x\,\delta x - i\kappa_y\,\delta y) \right.$$
$$\left. \times \int\limits_{0}^{\infty} \Big[ j_q(\kappa_x, \kappa_y, z'' - z - \delta z, \omega) G_{qj}^{kl}(\kappa_x, \kappa_y, z'', z', \omega) \Big] \tilde{G}_{ji}^{lk}(\kappa_x + k_x, \kappa_y + k_y, z', z, \omega)\, \mathrm{d}\kappa_x\, \mathrm{d}\kappa_y\, \mathrm{d}z'' \right\} \mathrm{d}z', \quad (1)$$

where $G_{qj}^{kl} = {}^{\parallel}G_{qj}^{kl} + {}^{\perp}G_{qj}^{kl}$ and $\tilde{G}_{ji}^{lk} = {}^{\parallel}\tilde{G}_{ji}^{lk} + {}^{\perp}\tilde{G}_{ji}^{lk}$ are the components of the Green's functions (tensors) in the $k$-space for the TE($\perp$) and TH($\parallel$) polarizations, and $j_i$ are the components of the transverse current spectrum in the field source (for brevity, the same notations are used for the transverse spectra, with a few exclusions). It is assumed that the repeated subscripts $q$ and $j$, which can be $x$, $y$, and $z$, are summed over (no summation takes place over the layer numbers $k$ and $l$) and the subscript $i$ can also be $x$, $y$, and $z$. The components of the Green's functions for the probing field are written as

$$
\begin{aligned}
{}^{\parallel,\perp}G_{qj}^{kl} = -\frac{k_0^2}{2\pi\omega k_\perp} g_{qj}^{\parallel,\perp}(k_x,k_y) \frac{T_{kl}^{\parallel,\perp}}{1 - R_{k,1}^{\parallel,\perp} R_{k,N+1}^{\parallel,\perp} \exp(2ik_{zk}d_k)} \\
\times \Big\{ \exp[ik_{zk}(z_k - z')] + R_{k,1}^{\parallel,\perp} \exp[ik_{zk}(z' - z_k + 2d_k)] \Big\} \\
\times \Big\{ \exp[ik_{zl}(z - z_l)] + \frac{z_{\text{in}}^{(l)\parallel,\perp} - z_l^{\parallel,\perp}}{z_{\text{in}}^{(l)\parallel,\perp} + z_l^{\parallel,\perp}} \exp[2ik_{zl}d_l - ik_{zl}(z - z_l)] \Big\}, \quad (2)
\end{aligned}
$$

$$
\mathbf{g}^{\parallel}(k_x,k_y) = \frac{1}{k_k k_l} \begin{pmatrix} \dfrac{k_x^2 k_{zl}}{k_\perp} & \dfrac{k_x k_y k_{zl}}{k_\perp} & -k_x k_\perp \\ \dfrac{k_x k_y k_{zl}}{k_\perp} & \dfrac{k_y^2 k_{zl}}{k_\perp} & -k_y k_\perp \\ -\dfrac{k_x k_\perp k_{zl}}{k_{zk}} & -\dfrac{k_y k_\perp k_{zl}}{k_{zk}} & \dfrac{k_\perp^3}{k_{zk}} \end{pmatrix}, \quad \mathbf{g}^{\perp}(k_x,k_y) = \frac{1}{k_{zk}k_\perp} \begin{pmatrix} k_y^2 & -k_x k_y & 0 \\ -k_x k_y & k_x^2 & 0 \\ 0 & 0 & 0 \end{pmatrix},
$$

$$
R_{k,N+1}^{\parallel,\perp} = \frac{z_{\text{in}}^{(k+1)\parallel,\perp} - z_k^{\parallel,\perp}}{z_{\text{in}}^{(k+1)\parallel,\perp} + z_k^{\parallel,\perp}}, \qquad T_{kl}^{\perp} = \prod_{i=k+1}^{l} \frac{z_{\text{in}}^{(i)\perp} + z_i^{\perp}}{z_{\text{in}}^{(i)\perp} + z_{i-1}^{\perp}} \exp(ik_{zi}d_i),
$$

$$
T_{kl}^{\parallel} = \sqrt{\frac{\varepsilon_k \mu_l}{\varepsilon_l \mu_k}} \prod_{i=k+1}^{l} \frac{z_{\text{in}}^{(i)\parallel} + z_i^{\parallel}}{z_{\text{in}}^{(i)\parallel} + z_{i-1}^{\parallel}} \exp(ik_{zi}d_i), \qquad z_{\text{in}}^{(k)\parallel,\perp} = \frac{z_{\text{in}}^{(k+1)\parallel,\perp} - iz_k^{\parallel,\perp}}{z_k^{\parallel,\perp} - iz_{\text{in}}^{(k+1)\parallel,\perp}} \frac{\tan(k_{zk}d_k)}{\tan(k_{zk}d_k)} z_k^{\parallel,\perp},
$$

$$
z_{\text{in}}^{(N+1)\parallel,\perp} = z_{N+1}^{\parallel,\perp}, \qquad z_k^{\parallel} = \frac{k_{zk}}{k_0 \varepsilon_k}, \qquad z_k^{\perp} = \frac{\mu_k k_0}{k_{zk}}, \qquad d_{N+1} = 0.
$$

The corresponding components for the scattered field are written as

$$
\begin{aligned}
{}^{\parallel,\perp}\tilde{G}_{ji}^{lk} = -\frac{k_0^2}{2\pi\omega k_\perp} \tilde{g}_{ji}^{\parallel,\perp}(k_x,k_y) \frac{\tilde{T}_{lk}^{\parallel,\perp}}{1 - \tilde{R}_{l,1}^{\parallel,\perp} \tilde{R}_{l,N+1}^{\parallel,\perp} \exp(2ik_{zl}d_l)} \\
\times \Big\{ \exp[-ik_{zl}(z_{l-1} - z')] + \tilde{R}_{k,N+1}^{\parallel,\perp} \exp[-ik_{zl}(z' - z_{l-1} - 2d_l)] \Big\} \\
\times \Big\{ \exp[-ik_{zk}(z - z_k)] + \frac{\tilde{z}_{\text{in}}^{(k)\parallel,\perp} - z_k^{\parallel,\perp}}{\tilde{z}_{\text{in}}^{(k)\parallel,\perp} + z_k^{\parallel,\perp}} \exp[-2ik_{zk}d_k + ik_{zk}(z - z_{k-1})] \Big\}, \quad (3)
\end{aligned}
$$

$$
\tilde{\mathbf{g}}^{\parallel}(k_x,k_y) = \frac{1}{k_k k_l} \begin{pmatrix} \dfrac{k_x^2 k_{zl}}{k_\perp} & \dfrac{k_x k_y k_{zl}}{k_\perp} & k_x k_\perp \\ \dfrac{k_x k_y k_{zl}}{k_\perp} & \dfrac{k_y^2 k_{zl}}{k_\perp} & k_y k_\perp \\ \dfrac{k_x k_\perp k_{zl}}{k_{zk}} & \dfrac{k_y k_\perp k_{zl}}{k_{zk}} & \dfrac{k_\perp^3}{k_{zk}} \end{pmatrix}, \quad \tilde{\mathbf{g}}^{\perp}(k_x,k_y) = \frac{1}{k_{zk}k_\perp} \begin{pmatrix} k_y^2 & -k_x k_y & 0 \\ -k_x k_y & k_x^2 & 0 \\ 0 & 0 & 0 \end{pmatrix},
$$

$$
\tilde{R}_{l,1}^{\parallel,\perp} = \frac{\tilde{z}_{\text{in}}^{(l-1)\parallel,\perp} - z_l^{\parallel,\perp}}{\tilde{z}_{\text{in}}^{(l-1)\parallel,\perp} + z_l^{\parallel,\perp}}, \qquad \tilde{T}_{lk}^{\perp} = \prod_{i=k}^{l-1} \frac{\tilde{z}_{\text{in}}^{(i)\perp} + z_i^{\perp}}{\tilde{z}_{\text{in}}^{(i)\perp} + z_{i+1}^{\perp}} \exp(ik_{zi}d_i),
$$

$$\tilde{T}_{lk}^{\parallel} = \sqrt{\frac{\varepsilon_l \mu_k}{\varepsilon_k \mu_l}} \prod_{i=k}^{l-1} \frac{\tilde{z}_{\rm in}^{(i)\parallel} + z_i^{\parallel}}{\tilde{z}_{\rm in}^{(i)\parallel} + z_{i+1}^{\parallel}} \exp(ik_{zi}d_i), \qquad \tilde{z}_{\rm in}^{(l)\parallel,\perp} = \frac{\tilde{z}_{\rm in}^{(l-1)\parallel,\perp} - iz_l^{\parallel,\perp}}{z_l^{\parallel,\perp} - i\tilde{z}_{\rm in}^{(l-1)\parallel,\perp}} \frac{\tan(k_{zl}d_l)}{\tan(k_{zl}d_l)} z_l^{\parallel,\perp},$$

$$\tilde{z}_{\rm in}^{(1)\parallel,\perp} = z_1^{\parallel,\perp}, \qquad z_l^{\parallel} = \frac{k_{zl}}{k_0 \varepsilon_l}, \qquad z_l^{\perp} = \frac{\mu_l k_0}{k_{zl}}, \qquad d_1 = 0,$$

$k_{zl} = \sqrt{k_l^2 - k_x^2 - k_y^2} = \sqrt{k_l^2 - k_\perp^2}$, $k_l = \sqrt{\varepsilon_l}\omega/c$, where $c$ is the speed of light and $d_i$ is the layer thickness.

Relationship (1) is an integral Fredholm equation of the first kind. On this basis, one can solve the inverse scattering problem in various formulations. The problem formulation is determined by choosing the parameters $\omega$, $z$, or $\delta\mathbf{r}$, which determine the depth selectivity of the kernel of this equation. In the multifrequency method, the data of measurements in the two-dimensional region $(x, y)$ at the level $z$ are used as functions of the frequency $\omega$ are used. If one uses the data of single-frequency scanning at various levels $z$ from the interface of the media (multilevel method), then the depth selectivity of the method will be related to the variation in the depth of near-field penetration to the inhomogeneity in the probed medium. One can also use the dependence of the kernel on the vector $\delta\mathbf{r}$ which determines the mutual position of the antennas. In practice, however, the multifrequency method is much simpler, and it is this method that is studied in the present paper for the case of an inhomogeneity in the half-space of a homogeneous medium.

Based on the results of the solution $\varepsilon_1(k_x, k_y, z)$ of inverse scattering problem (1), the desired three-dimensional distribution for the dielectric-permittivity deviation $\varepsilon_1(x, y, z)$ is determined by a two-dimensional inverse Fourier transform, whose visualization underlies the proposed method of electromagnetic tomography. To achieve its realization in practice, one should also allow for the influence of the transfer function of the measuring system.

## 3. THEORY OF TOMOGRAPHY AND HOLOGRAPHY

### 3.1. Tomography

Figure 1 shows the scheme of measurements of the field scattered by an inhomogeneity.

For the scheme under consideration, variations in the complex amplitudes of the received signal $s$ are expressed by the convolution of the instrument function $\mathbf{F}$ of a receiver with the scattered-field distribution $\mathbf{E}_1$:

$$s(\mathbf{r}_{\rm r}) = \int \mathbf{E}_1(\mathbf{r}')\mathbf{F}(x_{\rm r} - x', y_{\rm r} - y', z_{\rm r}, z')\,{\rm d}x'\,{\rm d}y'\,{\rm d}z', \quad (4)$$

where $\mathbf{r}_{\rm r} = (x_{\rm r}, y_{\rm r}, z_{\rm r})$ is the vector which determines the receiver position. Performing the two-dimensional Fourier transform over the transverse coordinates $x_{\rm r}$ and $y_{\rm r}$, from Eqs. (1) and (4) we obtain the one-dimensional integral equation for the transverse spectrum of the signal measured in the scanning process at the level $z_{\rm r}$:

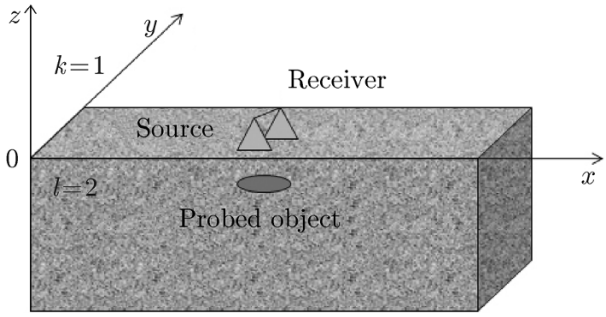

Fig. 1. Scheme of measurements by the method of subsurface microwave tomography.

$$s(k_x, k_y, \omega) = \int_{-\infty}^{0} \varepsilon_1(k_x, k_y, z')K(k_x, k_y, z', \omega)\,{\rm d}z', \quad (5)$$

$$K(k_x, k_y, z', \omega) = -4\pi^3 i\omega \int_{-\infty}^{0} \left\{ F_i(k_x, k_y, z, \omega) \iint_{-\infty}^{+\infty} \exp(-i\kappa_x\,\delta x - i\kappa_y\,\delta y) \right.$$

$$\times \int_0^\infty \Big[ j_i(\kappa_x, \kappa_y, z'' - z - \delta z, \omega)\, G_{ij}^{12}(\kappa_x, \kappa_y, z'', z', \omega) \Big] \tilde{G}_{ji}^{21}(\kappa_x + k_x, \kappa_y + k_y, z', z, \omega)\, \mathrm{d}\kappa_x\, \mathrm{d}\kappa_y\, \mathrm{d}z'' \Bigg\}\, \mathrm{d}z.$$

Equation (5) was used in the subsurface tomography algorithms developed in [3] and in tests of multifrequency microwave tomography in [4]. Equation (1) also allows one to determine the kernel of the three-dimensional integral for calculation of the measured signal in Cartesian coordinates within the Born approximation:

$$s(\mathbf{r}_\mathrm{r}, \omega) = \int \varepsilon_1(\mathbf{r}') K(x_\mathrm{r} - x', y_\mathrm{r} - y', z_\mathrm{r}, \omega, z')\, \mathrm{d}x'\ \mathrm{d}y'\ \mathrm{d}z'. \tag{6}$$

It is noted above that in our first experiments it was difficult to discern a subsurface object in the obtained two-dimensional distributions of the signal $s(x, y, \omega)$ against the background of strong noise, which was determined, as it turned out, by the scattering from the surface. However, it has been found that subsurface objects are clearly discernible when visualizing the signal transformed to the synthesized pulse

$$s(x_\mathrm{r}, y_\mathrm{r}, t) = \int_{\Delta\omega} s(x_\mathrm{r}, y_\mathrm{r}, \omega) \exp(i\omega t)\, \mathrm{d}\omega = \int \varepsilon_1(\mathbf{r}') K(x_\mathrm{r} - x', y_\mathrm{r} - y', z_\mathrm{r}, t, z')\, \mathrm{d}x'\, \mathrm{d}y'\, \mathrm{d}z', \tag{7}$$

where the time dependence can conveniently be replaced by the dependence the effective scattering depth $z_\mathrm{s}$ using the formula $t = -2z_\mathrm{s}\, \mathrm{Re}\sqrt{\varepsilon_0}/c$ (with allowance for the finite speed of light and the signal path towards the scattering element and back):

$$s(x_\mathrm{r}, y_\mathrm{r}, z_\mathrm{s}) = \int \varepsilon_1(\mathbf{r}') K(x_\mathrm{r} - x', y_\mathrm{r} - y', z_\mathrm{s}, z')\, \mathrm{d}x'\, \mathrm{d}y'\, \mathrm{d}z'. \tag{8}$$

Subsurface objects were easily observed by visualization of the pseudo-pulse amplitude $|s(x_\mathrm{r}, y_\mathrm{r})|$ at some values of $z_\mathrm{s}$, which increased as the object went deeper in the layer. The strong maximum of the pseudo-pulse, which was observed in the entire two-dimensional region of measurement $x_\mathrm{r}$ and $y_\mathrm{r}$, marked the value of $z_\mathrm{s}$ corresponding to the scattering from the surface. In order to use the informative part of the signal singled out in the pseudo-pulse during solving the inverse problem, initial equation (5) was transformed in a similar way:

$$s(k_x, k_y, t) = \int_{\Delta\omega} s(k_x, k_y, \omega) \exp(i\omega t)\, \mathrm{d}\omega, \tag{9}$$

where $t = -2z_\mathrm{s}\, \mathrm{Re}\sqrt{\varepsilon_0}/c$, and the integral is taken around the analysis band $\Delta\omega$. A new equation is obtained from formula (9), which connects the transverse spectra of inhomogeneity of the dielectric permittivity and the synthesized pseudo-pulse:

$$s(k_x, k_y, z_\mathrm{s}) = \int_{z'} \varepsilon_1(k_x, k_y, z') K_1(k_x, k_y, z', z_\mathrm{s})\, \mathrm{d}z',$$

$$K_1(k_x, k_y, z', z_\mathrm{s}) = K_1(k_x, k_y, z', t = -2z_\mathrm{s}\, \mathrm{Re}\sqrt{\varepsilon_0}/c),$$
$$K_1(k_x, k_y, z', t) = \int_{\Delta\omega} K(k_x, k_y, z', \omega) \exp(i\omega t)\, \mathrm{d}\omega. \tag{10}$$

Equation (10) was solved by the generalized disparity method for the complex-valued functions [3]. Finally, the solution of the tomography problem, i.e., the sought-for three-dimensional structure of the complex dielectric permittivity, is obtained from the solution of Eq. (10) in the $k$-space by using the inverse

Fourier transform:

$$s_1(x,y,z) = \iint\limits_{-\infty}^{+\infty} \varepsilon_1(k_x,k_y,z)\exp(ik_x x + ik_y y)\,\mathrm{d}k_x\,\mathrm{d}k_y. \tag{11}$$

### 3.2. Holography

In practice, subsurface inhomogeneities are internally homogeneous most frequently, i.e., $\varepsilon_1^0 = \text{const}$. For such objects, it is sufficient to solve a simpler problem of reconstruction of the shape of their surfaces, i.e., a computer holography problem [4], by using the solution of the tomography problem $\varepsilon_1(\kappa_x,\kappa_y,z)$ in the $k$-space, which was obtained from Eq. (10). For this purpose, we represent the object boundary in the cross-section $z = \text{const}$ as two functions $x_1(y,z)$ and $x_2(y,z)$, as is shown in Fig. 2.

Assuming that the functions $x_1(y,z)$ and $x_2(y,z)$ are single-valued, the solution of problem (10) can be represented as

$$\varepsilon_1(k_x,k_y,z) = \frac{1}{4\pi^2}\int\limits_{y_1}^{y_2}\int\limits_{x_1(y)}^{x_2(y)} \varepsilon_1^0\exp(-ik_x x - ik_y y)\,\mathrm{d}x\,\mathrm{d}y$$

$$= \frac{\varepsilon_1^0}{4\pi^2}\int\limits_{y_1}^{y_2}\exp(-ik_y y)\frac{\exp[-ik_x x_1(y)] - \exp[-ik_x x_2(y)]}{ik_x}\,\mathrm{d}y. \tag{12}$$

Then, we perform the Fourier transform over $k_y$,

$$\varepsilon_1(k_x,y',z) = \int\limits_{-\infty}^{+\infty}\varepsilon_1(k_x,k_y,z)\exp(ik_y y')\,\mathrm{d}k_y, \tag{13}$$

and obtain (having renamed $y' \to y$) the following complex-valued transcendental equation:

$$\varepsilon_1(k_x,y,z) = \frac{\varepsilon_1^0}{2\pi i k_x}\big\{\exp[-ik_x x_1(y,z)] - \exp[-ik_x x_2(y,z)]\big\}, \tag{14}$$

which is equivalent to a system of two real equations. The solution of the latter equations allows one to find the shape of an object as two functions $x_1(y,z)$ and $x_2(y,z)$ using the perturbation of the dielectric permittivity $\varepsilon_1(\kappa_x,y,z)$, which was obtained by solving Eq. (10). It should be noted that this system is overdetermined, since solutions can be found for each value of $k_x$. The overdetermination is due to the fact that the surface holography problem is simpler than the tomography problem. The freedom in selection of the component $k_x$ allows one to find ways to optimize the solving of Eq. (14), which opens up free scope for special research.

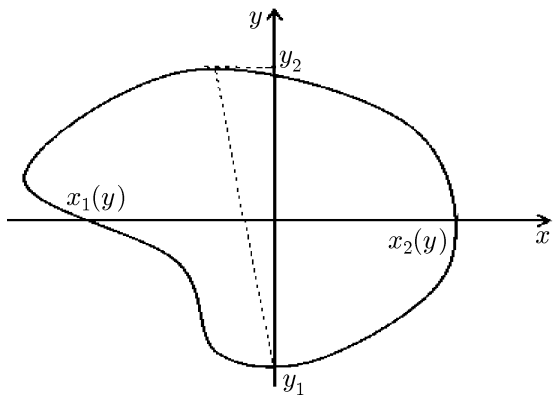


Fig. 2. Boundary of the probed object in the cross section $z = \text{const}$ in the form of the functions $x_1(y,z)$ and $x_2(y,z)$.

Our first optimization experiment was based on choosing the optimal value of this component. The results of such a simple optimization demonstrate that the best results are ensured by choosing $k_x \approx 2\pi/L_\mathrm{t}$, where $L_\mathrm{t}$ is the estimation of the typical object size, which is made on the basis of visualization of the transverse distribution of the pseudo-pulse. Note that an equation similar to Eq. (14) can be also obtained for the description of the surface by the functions $y_1(x,z)$ and

$y_2(x, z)$. Solving this equation allows one to supplement and verify the result of solving Eq. (14).

It should be emphasized that solving the tomography problem for objects with sharp boundaries on the basis of Eq. (11) does not allow reconstructing the object surface precisely, even neglecting the error of solution of this ill-posed problem. The matter is that discontinuous functions cannot be represented exactly by even an anyhow long Fourier series near the gradient-singularity points, although this representation is underlying for this tomography method. At such points, the Dini test for pointwise convergence is not satisfied, and the results will be inevitably distorted due to the Gibbs phenomenon. Allowing for errors, smoothing of stepwise functions during their reconstruction is inevitable. Therefore, if it is *a priori* known that the object is homogeneous, one should solve the problem of selecting the criterion for determination of the position of the sharp boundary in the smoothed solution. Solving Eq. (14) is such a mathematically consistent way of this selection.

## 4. MULTIFREQUENCY MICROWAVE TOMOGRAPHY AND HOLOGRAPHY

The developed theory was implemented in numerical algorithms and applied in the experiments, whose first results were published in [4]. The initial data for analysis were the results of measuring complex amplitudes of the signal at 801 frequencies in the range 1.7–7 GHz in the two-dimensional region $(x, y)$ over the probed subsurface inhomogeneity by using an "Agilent E5071B" vector network analyzer. The scanning system consisted of two identical, rigidly bound bow-tie antennas having dimensions of $3.8 \times 5.4$ cm and the distance $\delta y = 7.5$ cm between their centers in the bistatic configuration.

The current distribution on these wideband antennas is strongly localized near their centers. This fact ensures a very wide transverse spectrum over the wave vector, so that for a greater part of the range under analysis, the components with $\{k_x, k_y\} > 2\pi/\lambda$ are dominant. Then, according to Eq. (1), a wide near-field spectrum of the signal is formed, and it is possible to achieve a subwavelength resolution power. Theoretically, if one neglects data errors, the depth of such a high-resolution tomography region is unlimited. In practice, however, it will be determined only by the equipment sensitivity. Thus, in practice, due to attenuation of the near-field components in the probed medium, the resolution power decreases gradually and reaches the level determined by the Rayleigh limit.

### 4.1. Numerical simulation

Since it is impossible to obtain a simple relationship between the data error and the solution error in ill-posed problems and, moreover, the solution accuracy depends on the type of the reconstructed distribution, the mandatory stage of the study [6] is numerical simulation of the problem for a class of typical (or expected) probed objects by using the closed scheme (i.e., calculation of the scattered field for the modeled inhomogeneity, introduction of a random error, solution of the inverse problem with respect to these "measurement data," and comparison of the result with the parameters of the specified inhomogeneity).

To make it possible to scale and apply the results in different frequency bands, in the simulation we used dimensionless spatial scales specified in units of the minimum wavelength $\lambda_{\min}$ of the analysis, which was equal to $\lambda_{\min} \approx 4$ cm in our experiments. On this scale, the wavelength range of the analysis was equal to 1–4, and the sizes of the region of two-dimensional scanning in the $(x, y)$ plane was $7.5 \times 5$. The modeling was performed for the medium with dielectric permittivity $\varepsilon_0 = 4 + i\,0.5$. Other spatial scales of the above-described system were transformed in a similar way.

Since the quality of solving the inverse problems described by integral Fredholm equations of the first kind are decisively determined by the form of their kernel, the corresponding calculations were performed for the kernel of Eq. (5), where the multifrequency data were used directly, and for the kernel of Eq. (10) for the pulse synthesized on their basis. In Fig. 3, these kernels are shown for the couple of values $k_x = k_y = 2\pi/\lambda_{\min}$.

One can easily see in Fig. 3*a* that the contribution of the near-surface layer is dominant in the kernel of Eq. (5), which determines formation of the signal at individual frequencies. This explains noise contamination of the signal from embedded objects due to surface scattering, whereas the kernel for the

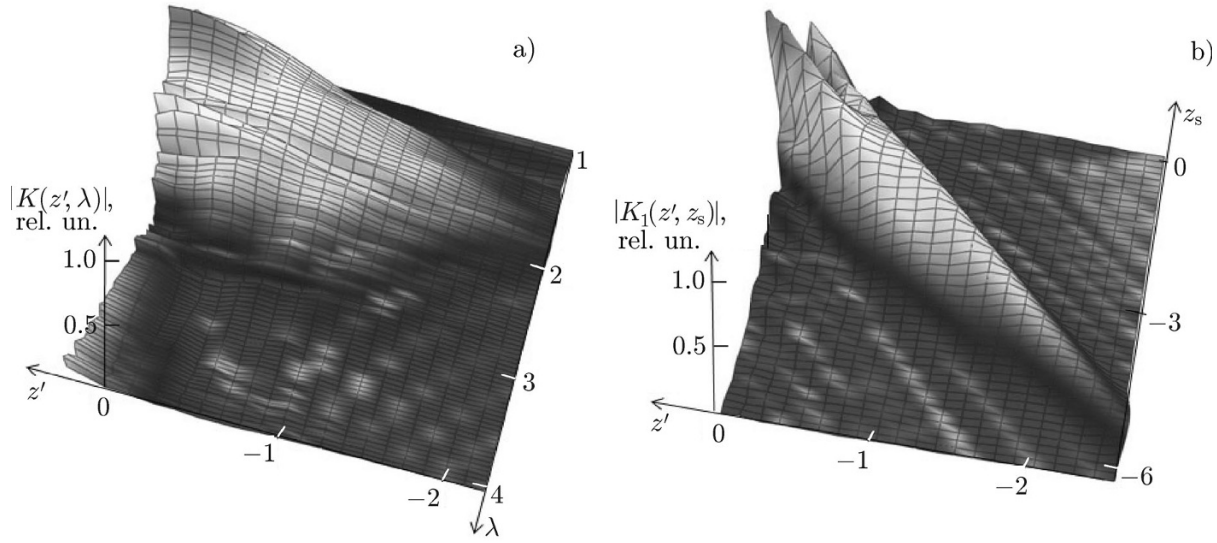


Fig. 3. Kernel of Eq. (5) at $k_x = k_y = 2\pi/\lambda_{\min}$ (*a*) and the corresponding kernel in Eq. (10) (*b*).

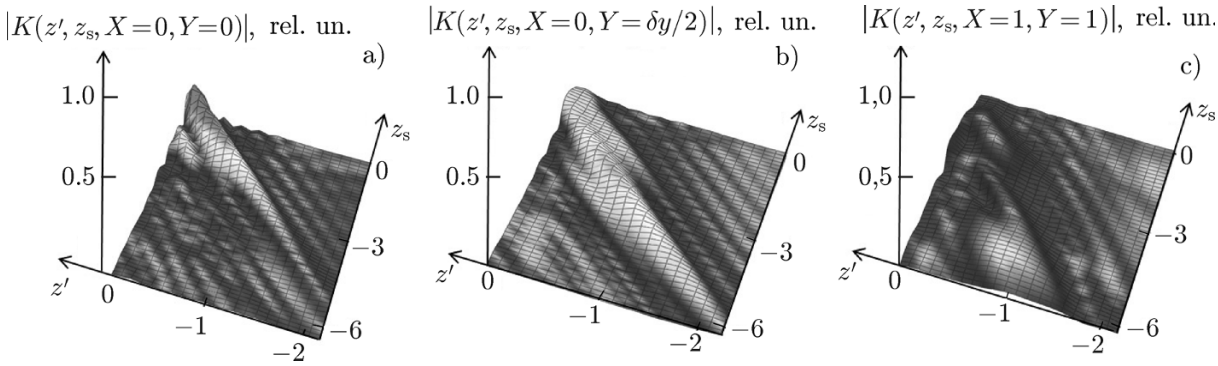


Fig. 4. Kernel of Eq. (8) at $X = Y = 0$ (*a*); $X = 0$, $Y = \delta y/2 = 0.9$ (*b*); and $X = Y = 1$ (*c*).

synthesized pseudo-pulse in Fig. 3*b* has maxima at different depths, at which the scattering objects located near them are detected. Such a kernel, due to its well-pronounced depth selectivity, forms the conditions which are drastically better for solving the inverse problem, since its properties approache those of a perfect kernel, i.e., a sequence of delta functions.

Since visualization of the pseudo-pulse amplitude $|s(x_r, y_r, z_s)|$ is used in the Cartesian coordinates in the scanning region rather than in the $k$-space for the purposes of detection and localization of a subsurface inhomogeneity, a comprehensive understanding of the pulse formation can be obtained by considering the kernel of Eq. (8), which is calculated by means of inverse Fourier transform of the kernel in Eq. (10):

$$K(X, Y, z_s, z') = \iint_{-\infty}^{+\infty} K_1(k_x, k_y, z', z_s) \exp(ik_x X + ik_y Y)\, \mathrm{d}k_x\, \mathrm{d}k_y,$$

where $X = x_r - x'$ and $Y = y_r - y'$.

Figure 4*a* shows the kernel of Eq. (8) for the receiver located directly over the scattering element. One can see, that as in Fig. 3*b*, high selectivity of the pseudo-pulse with respect to the depth position of the scattering element occurs. Figure 4*b* shows the kernel in the case where the scattering element is located in the middle between the receiving and transmitting antennas. In this case, the mirror component in the scattering increases, which is especially noticeable at a certain depth of the scattering element under the surface. On the whole, when the antenna is shifted off the vertical towards the scattering element, one

observes a decrease in the response at small depths of the scattering element and the response blurring, which is demonstrated in Fig. 4*c*.

Efficiency of the tomography and holography algorithms was studied numerically. The calculations of the scattered signal were performed in the integrated high-performance calculation environment of the metacluster of Lobachevsky State University of Nizhny Novgorod. The scattered field and the complex amplitudes of the received signal were calculated for the simulated objects, and a random, normally distributed error with a standard deviation of 10% was introduced to these quantities. The obtained "measurement data" were used for analysis. Figure 5 presents the results of tomography and holography of the simulated inhomogeneity, namely, a parallelepiped having sizes $1 \times 0.75 \times 0.5$ in relative units at the depth $z = -1$. These results were found from the solutions of Eqs. (10) and (14), respectively.

One can see that the algorithms show high efficiency and reconstruct the main parameters, shape, and position of the simulated inhomogeneity with good accuracy. It should be emphasized that each particular case of application of the proposed methods requires such a detailed study. However, numerical calculations are unable to reproduce all details of electrodynamics of an actual measuring system, especially when the objects are not low-contrast. Therefore, the question about the degree of reliability of the obtained results cannot be answered without accumulating experience from real experiments.

### 4.2. Experimental studies

The experiments showed that the proposed methods can be sufficiently efficient for weakly scattering dielectric objects. To a significant degree, this is due to the fact that when solving integral equation (5), one can use the "empirical" kernel obtained in an experiment with thin test objects having known shapes and located in small steps over the depth interval required for the analysis. The corresponding transverse spectrum of deviation of the dielectric permittivity of such an object can be represented as $\varepsilon_1(k_x, k_y, z') = \varepsilon_\mathrm{t}(k_x, k_y)\,\delta(z' - z_0)$, and kernel function is determined as $K_1(k_x, k_y, z_0, z_\mathrm{s}) = s(k_x, k_y, z_\mathrm{s}, z_0)/\varepsilon_\mathrm{t}(k_x, k_y)$.

If follows from the theory [3] that the integral representation of the signal is valid with a certain degree of accuracy beyond the framework of the Born approximation, as well. Therefore, this "experimental" kernel includes naturally the adjustment proposed in [3]. Such experimental studies were performed with the use of thin dielectric plates buried in a sand medium. Figure 6 shows kernel (10) of an integral equation for the transverse spectrum for the pseudo-pulse of the solved inverse problem, which was obtained for the pair of spectral components $k_x = k_y = 2\pi/4$ cm$^{-1}$, and the kernel in Eq. (8) for the pseudo-pulse in the Cartesian coordinates for the receiving antenna over the scattering elements ($X = Y = 0$).

One can see good agreement between the experimental kernels and the results of the theoretical calculations in Figs. 3 and 4, which demonstrates that the theory is adequate for the conditions under consideration.

The efficiency of the proposed methods was studied experimentally depending on the depth and shape of the probed objects. The depth dependence of the results was studied using foam-plastic test objects having dimensions $4 \times 4 \times 1$ cm and buried in sand.

Figure 7 (two upper and two lower rows of the panels) shows the results of measurements, i.e., visualized distributions of the scattered-signal amplitude at 5 out of 801 frequencies used in the analysis ($f = 1.7$, 3.025, 4.35, 5.675, and 7 GHz) in comparison with the images of the amplitudes of the synthesized pseudo-pulse at five values of the effective scattering depth ($z_\mathrm{s} = -6$, $-6.5$, $-7$, $-7.5$ and $-8$ cm) for an object at one of the depths ($z_\mathrm{t} = -7$ cm).

The results of measuring the scattered signal at individual frequencies, which are shown in Fig. 7 (upper rows), demonstrate how strongly the scattering from the object surface contaminates the signal scattered by the subsurface object with noise. At the same time, these components of the scattered signal are separate in the distributions of the pseudo-pulse synthesized on the basis of the multifrequency data (lower rows in Fig. 7), and the probed object becomes easily discernible in some interval of values of the parameter $z_\mathrm{s}$. One can note that the maximum scattering amplitude and the best sharpness of the image

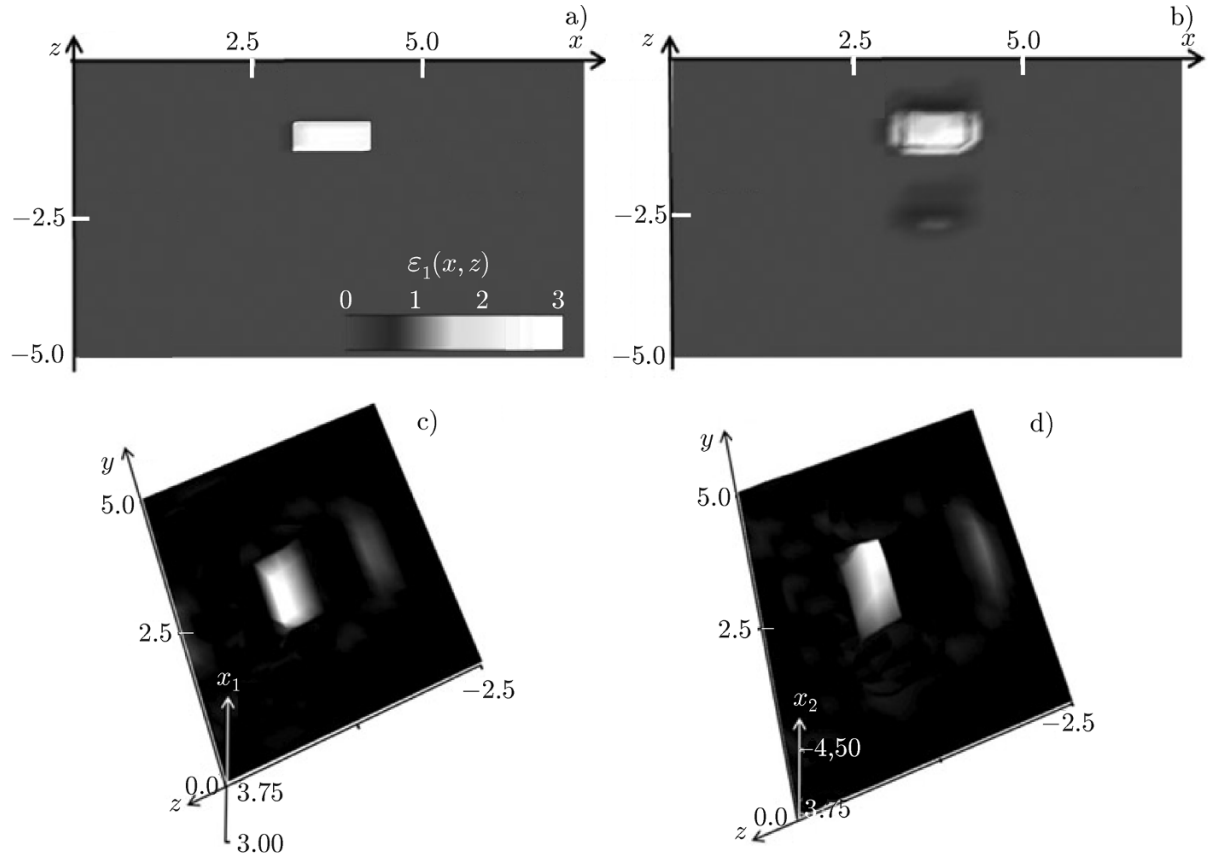


Fig. 5. Tomography simulation: the simulated object in the section $y = 2.5$ (*a*) and the tomography result (*b*) in the same section. Homography simulation: reconstruction of the object boundary using the function $x_1(y, z)$, where lighter regions correspond to smaller values of $x_2$ (*c*), and the function $x_2(y, z)$, where lighter regions correspond to greater values of $x_2$) (*d*).

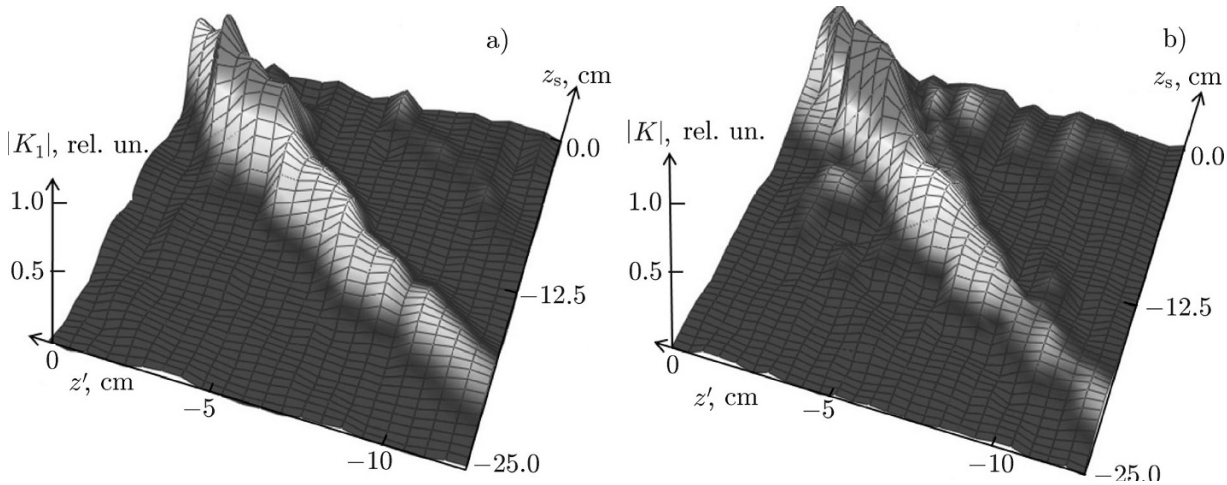


Fig. 6. "Experimental" kernel $K_1(k_x, k_y, z', z_s)$ in Eq. (10) for $k_x = k_y = 2\pi/4$ cm$^{-1}$ (*a*) and the kernel $K(X, Y, z_s, z')$ in Eq. (8) for $X = Y = 0$ (*b*).

are achieved if the effective scattering depth corresponds to the object depth. It allows one to estimate qualitatively the transverse and depth localization of the object, which is very important for solving the inverse problem and use the data from the interval of values of $z_s$, where the scattering by the object is stronger than noise (in the informative range), in solving Eq. (10).

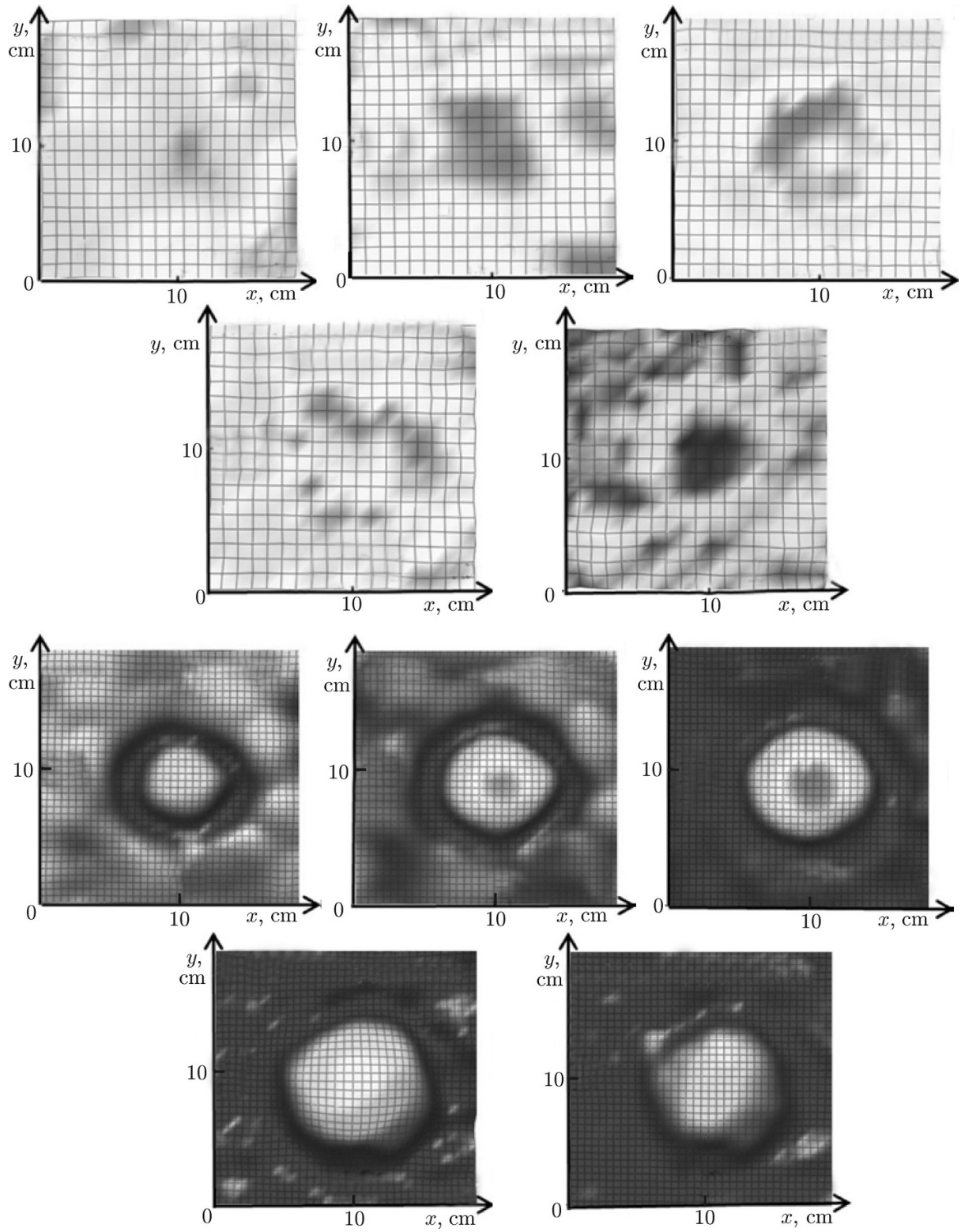


Fig. 7. Two upper rows: the signal amplitudes $|s(f)|$ in the analyzed region at five frequencies $f = 1.7$, 3.025, 4.35, 5.675, and 7 GHz (left to right and top to bottom) for an object at the depth $z_{\mathrm{t}} = -7$ cm; darker regions correspond to a higher signal level. Two lower rows: distributions of the pseudo-pulse amplitude $|s(z_{\mathrm{s}})|$ at the effective scattering depths $z_{\mathrm{s}} = -6$, $-6.5$, $-7$, $-7.5$, and $-8$ cm (left to right and top to bottom); lighter regions correspond to a higher amplitude of the pseudo-pulse.

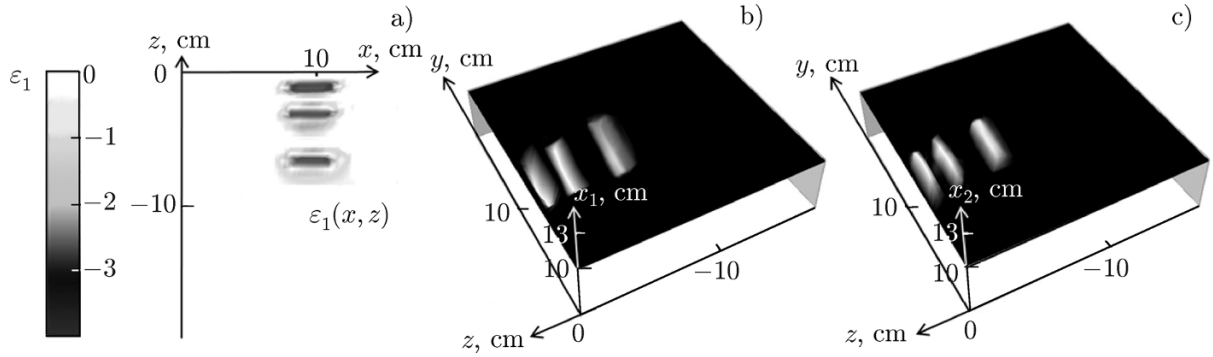


Fig. 7 (continued). Results of subsurface microwave tomography (vertical section of the dielectric-permittivity. deviation at $y = 10$ cm for objects at the depths $z_t = -1$, $-3$, and $-7$ cm) (*a*). Visualization of the holographic analysis, i.e., the surface of inhomogeneities at the depths $z_t = -1$, $-3$, and $-7$ cm, which was determined from Eq. (14) as the two functions $x_1(y,z)$ and $x_2(y,z)$, where lighter regions correspond to smaller values of $x_1$ and greater values of $x_2$ (*b*), (*c*)

Figure 7 (continued) shows the results of holographic and tomographic analysis based on solving Eqs. (10) and (14) for an object at the depths $z_t = -1$ $-3$, and $-7$ cm. In this analysis, we used the distributions of the pseudo-pulse in the range $-0.5 \le z_s$ [cm] $\le -10$. The region of analysis in the $k$-space was specified as $-8\pi \le k_x[\text{cm}^{-1}] \le 8\pi$ and $-8\pi \le k_y[\text{cm}^{-1}] \le 8\pi$. The results demonstrate good (no worse than 20%) accuracy of determination of the parameters, position, and shape of the objects at different depths.

One can see that as the object is shifted towards the near-zone boundaries for the maximum wavelength, the object image gradually blurs, but on the whole, the quality of tomographic and holographic analysis is still rather satisfactory.

The method was studied for objects having different shapes and compositions. Figure 8 shows the results of studies for a spherical epoxide object of 6 cm in diameter buried at the depth $z_t = -4$ cm (a billiard ball), whose dielectric permittivity is close to that of the surrounding sand environment ($\varepsilon \approx 5$)

One can see that in the case of a rather small difference between the dielectric permittivities of the object and the medium, the visualized object is less discernible compared with the case shown in Fig. 7. However, this small difference in the dielectric permittivities ensure better fulfillment of the Born approximation, and the results demonstrate good quality of reconstruction of the shape and determination of the position of the probed low-contrast dielectric object.

## 5. CONCLUSIONS

Based on numerical simulations and experimental studies, we demonstrated efficiency of the developed methods of microwave tomography and holography, as well as their good transverse (to the line of sight) and depth resolution power for subsurface inhomogeneities having low contrast in terms of their dielectric permittivities. At the same time, much effort should be focused on studies of the limits of applicability of these methods for higher-contrast object complex-shape objects, and media with significant absorption and high dielectric permittivities, such as, e.g., water or biological media. Apparently, this will require new approaches to solving the inverse problem beyond the limits of applicability of the Born approximation, as well as transition to a longer-wavelength band. However, such studies are very promising for applications in defectoscopy, analysis of ground penetrating radar data, and, especially, in medical applications, where low-contrast manifestations of various pathologies are of enhanced interest. The developed methods can be transferred without significant changes in the algorithms to the problems of geomagnetic or acoustic sounding (see, e.g., [1, 7]).

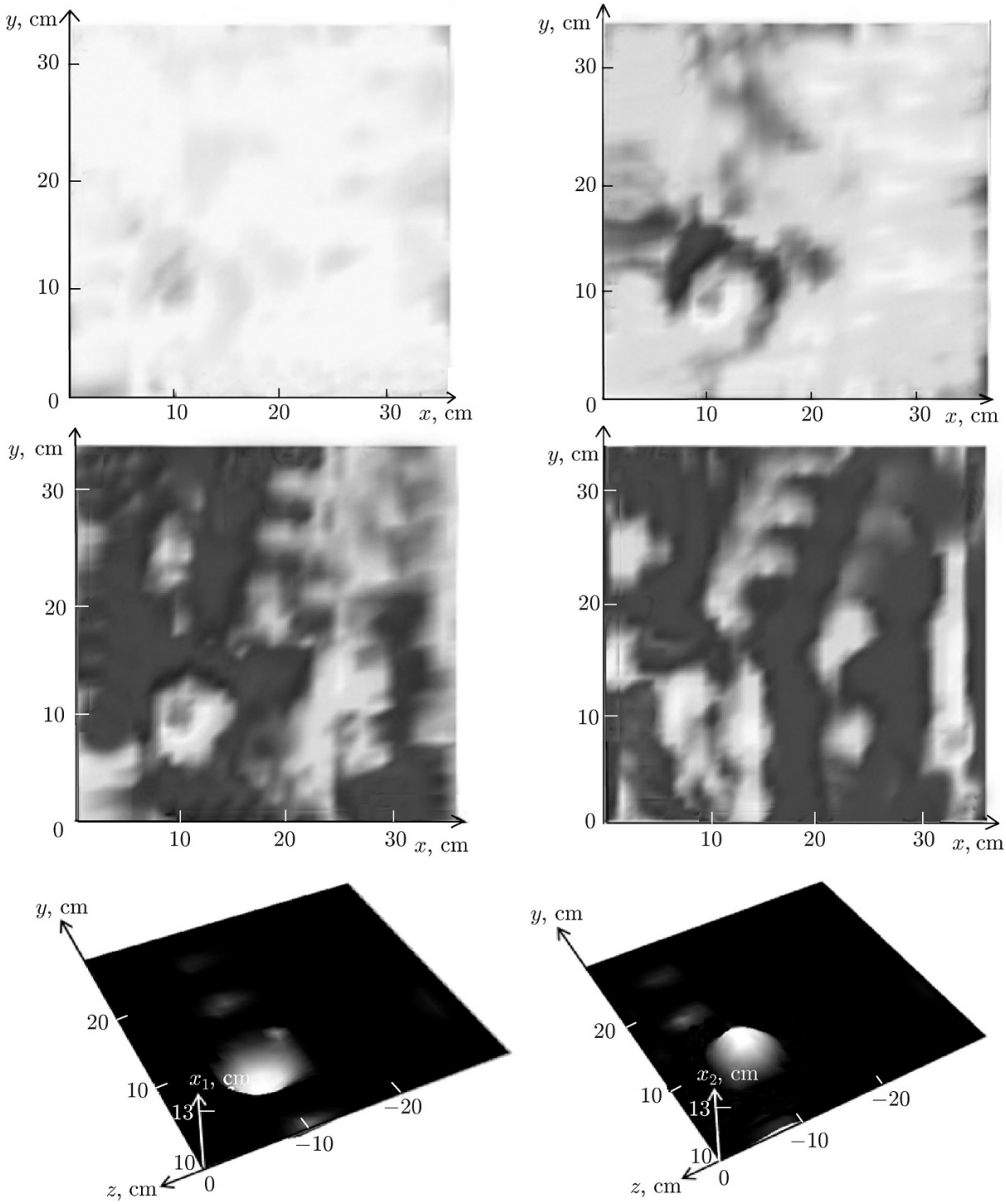


Fig. 8. Two upper rows: distributions of the pseudo-pulse amplitude $|s|$ for the effective scattering depths $z_s = -4$, $-5$, $-6$, and $-10$ cm (left to right and top to bottom). The lower row: visualization of the holographic analysis, i.e., the object surface determined from Eq. (14) as two functions $x_1(y, z)$ and $x_2(y, z)$. Lighter regions correspond to smaller values of $x_1$ and greater values of $x_2$.

This work was supported by the Russian Foundation for Basic Research (project Nos. 12–02–90028-Bel, 13–07–97028_p_povolzhie, and 13–02–12155_ofi_m), the Belarusian Republican Foundation for Fundamental Research (project No. T12R–133), and program IV.13 of the Division of Physical Sciences of the Russian Academy of Sciences.

**REFERENCES**


1. K. P. Gaikovich, *Phys. Rev. Lett.*, **98**, No. 18, 183902 (2007).
2. P. S. Carney, V. A. Markel, and J. C. Schotland, *Phys. Rev. Lett.*, **86**, No. 26, 5874 (2001).
3. K. P. Gaikovich and P. K. Gaikovich, *Inverse Problems*, **26**, No. 12, 125013 (2010).
4. K. P. Gaikovich, P. K. Gaikovich, Ye. S. Maksimovitch, and V. A. Badeev, *Phys. Rev. Lett.*, **108**, No. 16, 163902 (2012).
5. V. V. Razevig, S. I. Ivashov, A. P. Sheyko, et al., *Electromagn. Res. Lett.*, **1**, 173 (2008).
6. K. P. Gaikovich, *Inverse Problems in Physical Diagnostics*, Nova Science Publishers, New York (2004).
7. P. K. Gaikovich, A. I. Khil'ko, and K. P. Gaikovich, *Radiophys. Quantum Electron.*, **54**, No. 6, 390 (2011).